JACS
JOURNAL OF THE AMERICAN CHEMICAL SOCIETY
pubs.acs.org/JACS
Article

Tertiary Hierarchical Complexity in Assemblies of Sulfur-Bridged Metal Chiral Clusters

Haixiang Han, Yuan Yao, Anuj Bhargava, Zheng Wei, Zhichu Tang, Jin Suntivich, Oleksandr Voznyy, and Richard D. Robinson*

Cite This: J. Am. Chem. Soc. 2020, 142, 14495−14503
Read Online
ACCESS | Metrics & More | Article Recommendations | Supporting Information

ABSTRACT: Self-assembly of three-dimensional structures with order across multiple length scales—hierarchical assembly—is of great importance for biomolecules for the functions of life. Creation of similar complex architectures from inorganic building blocks has been pursued toward artificial biomaterials and advanced functional materials. Current research, however, primarily employs only large, nonreactive building blocks such as Au colloids. By contrast, sulfur-bridged transition metal clusters (<2 nm) are able to offer more functionality in catalytic and biochemical reactions. Hierarchical assembly of these systems has not been well researched because of the difficulty in obtaining single-phase clusters and the lack of suitable ligands to direct structure construction. To overcome these challenges, we employ a rigid planar ligand with an aromatic ring and bifunctional bond sites. We demonstrate the synthesis and assembly of 1.2 nm sulfur-bridged copper (SB-Cu) clusters with tertiary hierarchical complexity. The primary structure is clockwise/counterclockwise chiral cap and core molecules. They combine to form clusters, and due to the cap−core interaction (C−H···π), only two enantiomeric isomers are formed (secondary structure). A tertiary hierarchical architecture is achieved through the self-assembly of alternating enantiomers with hydrogen bonds as the intermolecular driving force. The SB-Cu clusters are air stable and have a distribution of oxidation states ranging from Cu(0) to Cu(I), making them interesting for redox and catalytic activities. This study shows that structural complexity at different length scales, mimicking biomolecules, can occur in active-metal clusters and provides a new platform for investigation of those systems and for the design of advanced functional materials.

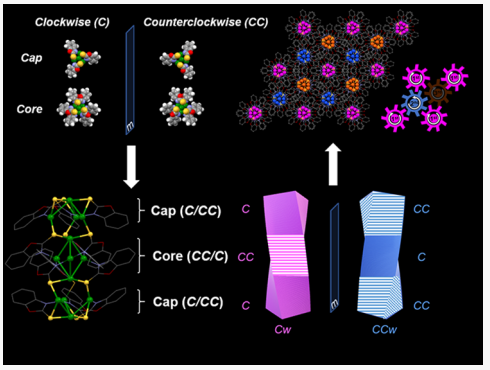

INTRODUCTION

In nature, primary, secondary, or more complex structures can form through self-folding or intermolecular interactions found in the diverse biomolecules of DNA, RNA, or proteins. For example, typical secondary structure can appear in proteins through ordered helical twisting (i.e., α-helix) of their primary structure (linear sequences of the amino acids) formed from intramolecular hydrogen bonds, and higher-level complexity from hierarchical assembly can have structures, including quaternary structure, as occurs in rRNA (rRNA).[1,2] In biochemistry, complexity has been achieved by taking advantage of the self-assembly behavior of biomolecules to create synthetically derived supramolecular assemblies.[3−5] Hierarchical assemblies of well-patterned structural organization at different levels, such as those commonly occurring in biomolecule systems, afford much richer functionality than randomly distributed units. Achieving hierarchical structural complexity that mimics natural living systems from lab-synthesized nanoscale building blocks is a grand challenge that promises to unlock secrets of bioformations and the potential to deliver novel applications.[6,7] Nanoscience researchers have pursued complexity through the assembly of clusters (<2 nm)[8−12] and relatively larger nanoparticles (NPs) (>2 nm) formed by entropy,[13] electrostatic interactions,[14] or large biomolecule linkers like DNA or polymers as a template.[15−19] While these achievements have progressed the field, there are still significant challenges, including creation of self-directed, atomically uniform hierarchical architectures and introduction of chirality into the structures.

Achieving complexity in NPs that mimics biomolecules is extremely rare with, to the best of our knowledge, only one report of hierarchical assemblies using Au NPs.[20] In this report, large (2.2 nm, 246 core atoms) closed-spherical metallic Au NPs form a hierarchical assembly via a C−H···π interaction. Progressing from these large, solid-core precious metals to smaller clusters made from more active metal−sulfur complexes can advance the field further toward biomaterials

Received: May 5, 2020
Published: July 27, 2020

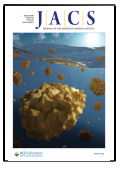

https://dx.doi.org/10.1021/jacs.0c04764
J. Am. Chem. Soc. 2020, 142, 14495−14503

and enable additional properties, such as luminescence or redox activity. However, single-phase metal−sulfur clusters are difficult to synthesize with atomic regularity because the metal−sulfur bonds are flexible and encourage a broad diversity of atomic arrangements,[21] resulting in nonuniform or multiphase products. Equally, metal−sulfur compounds are not as stable as noble metal clusters or particles.[21] The use of copper is promising because of the lower cost and intriguing optical and electrocatalytical properties, as well as the newly emerging bioapplications,[22−26] but determination of precise crystal structures from copper clusters is rare because copper is vulnerable to oxidation from air exposure and the difficulties with single-crystal growth.[27]

To overcome these challenges, we employed 2-mercaptobenzoxazole (MBO) as our surfactant ligand. The choice of MBO is based on three major considerations. (1) The rigidity of the structure. The small MBO ligand has neither long, flexible tails nor branched groups, and the sp^2 hybridization of the C and N atoms make all atoms planar. Therefore, the rigid MBO reduces the degrees of freedom for structure types. (2) The bifunctional binding through both S and N atoms which immobilizes the ligand onto the surface of the nanocluster, preventing rotating or swinging. In addition, the bifunctional binding enables MBO to bind at a tilted angle, enabling aligned patterns for the organic ligands. (3) The aromatic rings as well as the electronegative O and N atoms in the MBO ligand afford rich sources for potential interactions, such as hydrogen bonding or $\pi-\pi$ stacking, across ligands, which are potential driving forces to form long-range intermolecular order.[20] Successful application of the MBO ligand to synthesize the atomically precise, structurally stable non-noble cluster would greatly expand the range of organic ligands with common structure characteristics to prepare new Cu-based nanoclusters.

Here, we demonstrate the first atomically precise structure of hierarchical architecture built from chiral 1.2 nm sulfur-bridged copper (SB-Cu) clusters. The SB-Cu cluster units feature a unique cap−core−cap structure with the Cu atoms connected by a mixture of metal−metal bonds and bridging sulfur atoms from the organic ligands, enabling a diversity of oxidation states for the Cu. The ligand bonding endows distinct chirality of either clockwise (*C*) or counterclockwise (*CC*) rotation for each cap and core, and ultimately, intramolecular interaction (C−H···π) results in the formation of only two cap−core−cap enantiomeric configurations (*C*−*CC*-*C* or *CC*-*C*−*CC*). Interestingly, the cap component of the cluster has a similar function as the capsid of a virus,[28] guiding the interaction between clusters and organization of the architecture. In addition, due to the inhomogeneous distribution of oxidation states, some of the Cu atoms in the clusters possess partial Cu(0) character but are surprisingly stable for more than 3 months in the open air. The SB-Cu clusters show excellent durability in the oxygen reduction reaction (ORR), which may be a result of their intrinsic structural stability, are electrocatalytically active for carbon dioxide reduction, and show photoluminescence in the visible range. This work is the first to illustrate that the intra/intermolecular interactions can be present in metal clusters and guide structural hierarchy to increasingly complex organizations, including tertiary structure, resembling biomolecules.

RESULTS AND DISCUSSION

The SB-Cu clusters were synthesized through a borohydride reduction of copper salts in the presence of 2-mercaptobenzoxazole (MBO) ligands, modified from previously reported methods[27] (see methods in Supporting Information). Briefly, $NaBH_4$ in acetonitrile was rapidly added into a suspension of $CuCl_2$ and MBO, and the resultant solution was stirred for 1 h. The solution underwent a color change from brown to colorless to brown again. After washing and drying, the yield of the phase-pure cluster was ∼43% based on the $CuCl_2$ mass. UV−vis absorption of the SB-Cu clusters shows a prominent peak at 333 nm and a very weak peak around 430 nm (SI, Figure S4). The SB-Cu clusters emit blue fluorescence with the main photoluminescence peak at 379 nm and weaker shoulders at 370 and 410 nm (SI, Figure S5). The quantum yield is 8.9%, suggesting a dominant nonradiative decay process, and the fluorescence lifetime of the 379 nm peak is 2.79 ns (SI, Figure S6). The SB-Cu clusters are diamagnetic, as confirmed by ^{1}H NMR spectroscopy (SI, Figure S9 and Table S2), precluding the presence of Cu^{2+}. The SB-Cu clusters are very stable in the open air, displaying identical NMR, XRD, and fluorescence attributes after 3 months exposure in air (SI, Figures S7 and S8, Table S1).

Block-shaped, bright yellow high-quality single crystals of SB-Cu clusters were grown from a saturated acetonitrile solution at room temperature, enabling atomically precise identification of the structure through single-crystal X-ray diffraction (resolution 0.86 Å) (see SI for more details) (Figure 1). Each cluster consists of 13 copper atoms and 12 MBO organic ligands that bind to the metals through their S and N atoms. ^{1}H NMR (SI, Figure S9) shows two sets of proton peaks that match the MBO ligand binding configuration seen in the X-ray data, confirming the purity of the bulk product. The morphology of the inorganic metal framework is prolate (∼1.2 nm in length by ∼0.3 nm in diameter, considering only the Cu) and of point group C_3 (Figure 1a). Unlike the 13-atom icosahedron—commonly observed in gold and silver[29]—the SB-Cu cluster is formed from a novel cap−core−cap configuration with a Cu_5 bipyramidal core sandwiched by two Cu_4 trigonal pyramidal caps. In the Cu_4 caps, the Cu−Cu bond lengths from the apex to the three base Cu atoms are equally 2.737 Å, while the distance between the Cu atoms on all three edges in the triangular base are 3.606 Å in length, which exceeds the van der Waals length of 2.80 Å for Cu−Cu bond (SI, Figure S11, Table S5).[30,31] This suggests a metallic bond between the apex and three base atoms but nonbonding interactions between the three base atoms. The Cu_5 core unit geometry is bipyramidal, constructed by two apex coppers and three copper atoms aligned in a triangular plane that is centered between the apex coppers (SI, Figure S12). The Cu−Cu bond distances between each apex Cu and the three middle coppers are equal at 2.714 Å, but the distance between the three triangular coppers (2.899 Å) exceeds the van der Waals limit, so no metallic bond is formed (SI, Table S8). Because of the different coordination environments and geometries, the Cu−Cu bond distances in our SB-Cu clusters range from 2.714 to 2.737 Å, which are longer than those in metallic Cu (2.55 Å) but shorter than the van der Waals bond length (2.898 Å). The narrow distribution of the Cu−Cu bond distances can be attributed to the small dimensions of the cluster and its highly symmetric structure. This range of Cu metal bonds is consistent with that reported for other copper clusters (SI, Table S10). It is interesting to note that the Cu_4 caps and the Cu_5 core are not directly connected through Cu metallic bonds but are linked by μ_2-S from a MBO ligand (SI, Figure S10).

https://dx.doi.org/10.1021/jacs.0c04764
J. Am. Chem. Soc. 2020, 142, 14495−14503

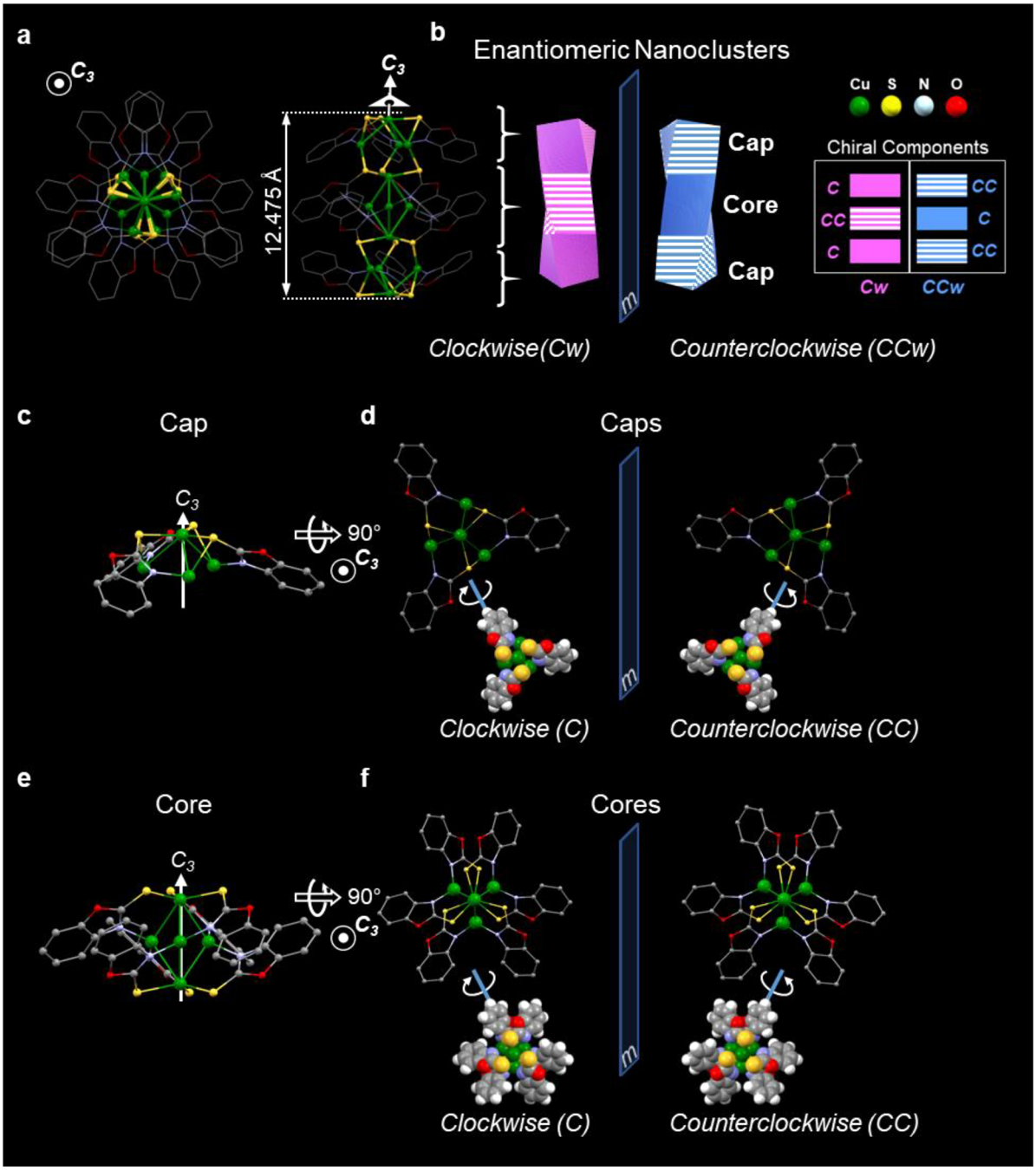

Figure 1. SB-Cu cluster structure derived from single-crystal X-ray diffraction. (a) (Left) Top view, parallel to the C_3 axis, and (right) side view, perpendicular to the C_3 axis, of the SB-Cu cluster structure. Full view structure and bond distances and angles can be found in the SI, Figures S10−S12, Tables S4−S9. (b) Each of the three components of the SB-Cu clusters (cap, core, cap) possesses either clockwise (*C*) or counterclockwise (*CC*) chirality with both caps in a cluster having the same chirality and the core opposite chirality. For the full SB-Cu cluster there are only two configurations, *C*−*CC*−*C* and *CC*−*C*−*CC* (cap−core−cap), resulting in two enantiomeric isomers denoted as *Cw* and *CCw*, respectively. Side view (c) and top view (d) of the structure of the $Cu_4(MBO)_3$ cap. (d) MBO ligand binding configuration of the cap is rotated with respect to the C_3 axis, forming enantiomers of either clockwise (*C*) or counterclockwise (*CC*) chirality. Side view (e) and top view (f) of the $Cu_5(MBO)_6$ core structure. (f) MBO binding forms enantiomeric $Cu_5(MBO)_6$ cores with rotational direction either clockwise (*C*) or counterclockwise (*CC*) with respect to the C_3 axis. *m* represents the mirror planes in b, d, and f. For clarity, carbon, oxygen, and sulfur atoms are drawn in wireframe style and hydrogen atoms are omitted.

The precision of the single-crystal X-ray diffraction reveals that the structural units of the single crystal are comprised of two enantiomeric isomers derived from the asymmetric bonding of the MBO to the caps ($Cu_4(MBO)_3$) and core ($Cu_5(MBO)_6$) (Figure 1b). In the $Cu_4(MBO)_3$ cap, each MBO ligand binds to a base Cu through an N atom (Cu−N = 1.964 Å) while the S atom links to an adjacent Cu and to the apex Cu (Cu_{base}−S = 2.328 Å and Cu_{apex}−S = 2.262 Å) (Figure 1c and SI, Figure S11). The bonding configuration produces a tilting of the ligand plane relative to the C_3 axis of the Cu_4 pyramid, which imbues chirality on the $Cu_4(MBO)_3$ cap motif, like a propeller, with either a clockwise (*C*) or a counter-

https://dx.doi.org/10.1021/jacs.0c04764
J. Am. Chem. Soc. 2020, 142, 14495−14503

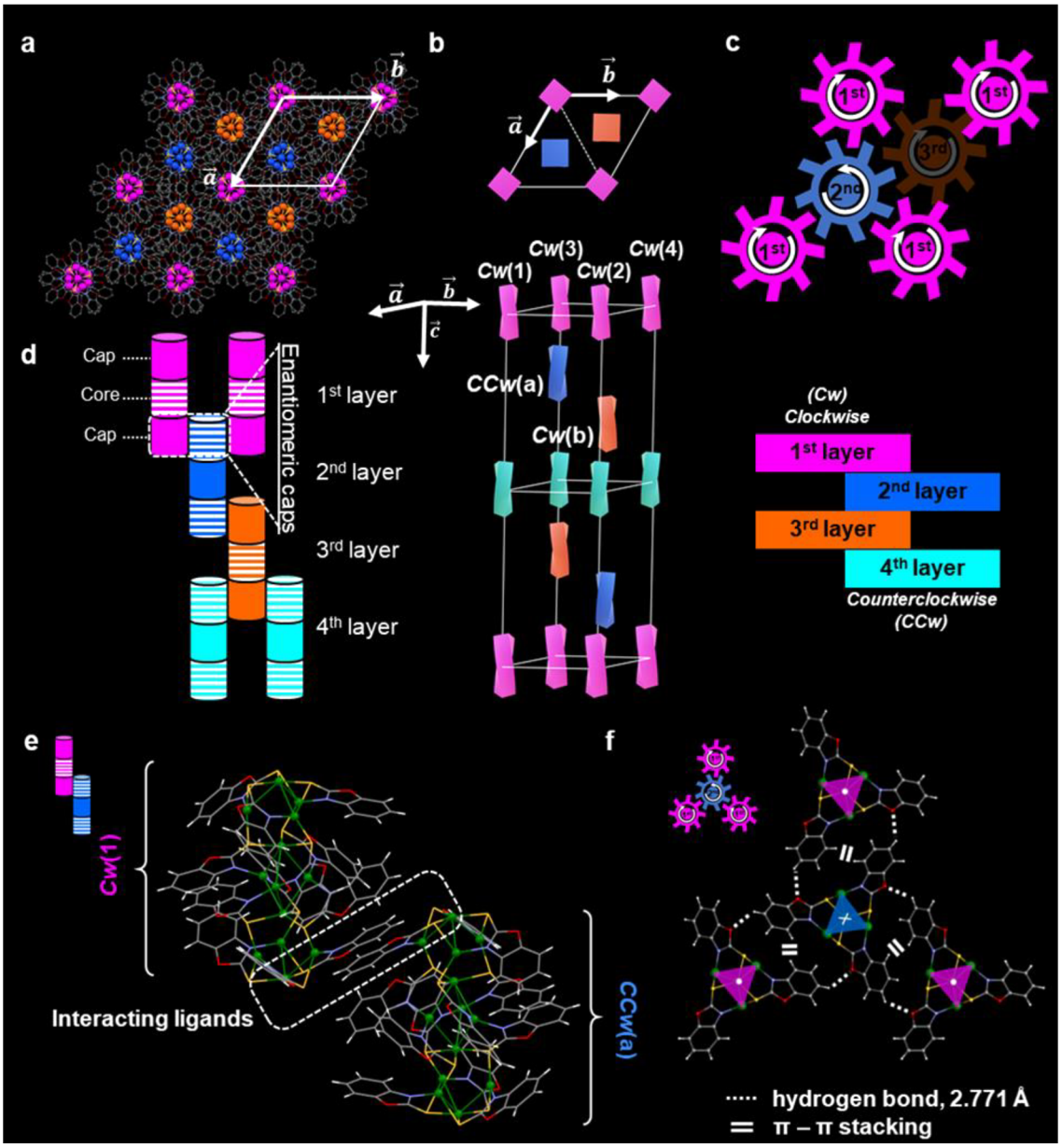

Figure 2. Single-crystal packing structure and chirality of SB-Cu clusters. (a) Viewed parallel to the *c* axis with the unit cell outlined. Top layer is *Cw* (magenta, see legend), and subsequent layer is *CCw* (blue). (b) Schematic representation of the single-crystal unit cell viewed (top) parallel to the *c* axis and (bottom) in perspective. There are 6 clusters in each unit cell, and each *ab*-plane layer has opposite chirality. (c) Schematic showing different chirality of layers, as viewed down the *c* axis. Enantiomeric clusters interact with an opposite chirality pair, as gears. (d) 2D schematic representation of the cap−cap interactions forming the hierarchical structure (solid and striped areas represent clockwise and counterclockwise components, respectively). Two clusters align through their caps of opposite chirality. (e) Stacking interaction of two representative SB-Cu clusters. (f) Ligand−ligand interactions of clusters in different layers (dot and cross represent the bottom cap of the first layer and the top cap of the second layer, respectively).

clockwise (*CC*) arrangement (Figure 1d). Importantly, both $Cu_4(MBO)_3$ caps in each cluster always assume identical chirality. The MBO attachments to the core $Cu_5(MBO)_6$ (Figure 1e) are similar to that of the caps, with all N atoms attached to the midsection triangular plane coppers, while the S atoms attach to one apex Cu and also to a base Cu from an adjacent cap (Figure 1a and SI, Figure S12).

The ligands attach in a twisted fashion relative to the vertical axis, similar to the MBO on the caps, imparting either a *C* or a *CC* chirality to the $Cu_5(MBO)_6$ core (Figure 1f). Their attachment alternates between the upper and the lower apex coppers with three nearly parallel pairs (the dihedral angle between two ligand planes is 3.96°) aligned in C_3 symmetry. The distance between the centers of mass for any two nearly parallel pairs of ligands is 3.312 Å, suggesting a novel intramolecular parallel-displaced $\pi-\pi$ stacking interaction (SI, Figure S13). Similar attractive, noncovalent interactions play a significant role in biomolecules, such as DNA and RNA,[32,33] but have not been used to create highly organized structure for clusters at atomic precision.

The anatomy of the full SB-Cu cluster (Figure 1a) is a sandwich construction with two chiral $Cu_4(MBO)_3$ caps and a chiral $Cu_5(MBO)_6$ core; however, the core chirality is always opposite to the two caps due to the intramolecular C−H···π

https://dx.doi.org/10.1021/jacs.0c04764
J. Am. Chem. Soc. 2020, 142, 14495−14503

interaction (SI, Figure S14), mimicking a secondary structure formation of biomolecules. Two different configurations exist for the SB-Cu cap−core−cap arrangement: *CC*−*C*−*CC* and *C*−*CC*−*C* (Figure 1b). Hereafter, we define the chirality of a SB-Cu cluster as *Cw* if its two caps are in the clockwise rotational direction (*C*−*CC*−*C*) and *CCw* for its enantiomer (*CC*−*C*−*CC*).

The presence of enantiomers enables the clusters to form an organized, hierarchical framework (Figure 2) with adjacent layers along the *c* axis having opposite chirality. The SB-Cu clusters crystallize into the trigonal space group $R\bar{3}c$ (167) with six clusters in each unit cell (Figure 2b and SI, Figure S15). The top and bottom *ab* planes of the unit cell have four *Cw* clusters aligned in plane at the corners of the cell, while located at the midpoint of the *c* axis are four clusters with the opposite chirality (*CCw*). At the center of each triangular region defined by the upper four *Cw* clusters is a *CCw* cluster, which is offset along the *c* axis, so that the top caps of one set align with the bottom caps of the other; for example, *CCw*(a) is situated below the plane formed by *Cw*(1)−(3) with the bottom caps of *Cw*(1), *Cw*(2), and *Cw*(3) aligning with the top cap of *CCw*(a) (Figure 2b and 2c). In this way, the SB-Cu clusters self-assemble into a lattice where neighboring *ab*-plane layers have clusters with opposite chirality, repeated throughout the entire single crystal (Figure 2d).

The assembly of alternating chiral clusters is a result of the ligand−ligand interactions between the top cap of one cluster and the bottom caps of its neighbors (Figure 2e). Examination of the ligand−ligand interaction (Figure 2f) unambiguously shows that the O···H hydrogen bonds act as driving forces for this phenomenon. For example, for the cluster shown in Figure 2b, each of the three top cap ligands of *Cw*(a) connects with two surrounding ligands from the bottom caps of *CCw*(a) connects with two surrounding ligands from the bottom caps of *Cw*(1), *Cw*(2), and *Cw*(3) through its oxygen and hydrogen atoms, forming two hydrogen bonds (length = 2.771 Å) (Figure 2e and 2**f**, also see SI, Figure S16). This attractive interaction is consistent with the tilting of the MBO ligands relative to the main cluster central C_3 axis to enable the overlap between neighboring cluster's MBO ligands. Such parallel stacking, directed by the hydrogen bonds, in turn, maximizes the packing density to further stabilize the overall interlocking mode. The resultant overall geometry constructed by these four clusters features the same C_3 symmetry, which is important for creating an ordered assembly (SI, Figures S17 and S18).[20]

The structural anatomy of this unique SB-Cu cluster clearly reveals the similarity in the structure complexity at different levels when compared with biomolecules. The cap and core components each constructed with metal−metal bonds display independent chirality, playing a role as a primary structure like those defined in a biosystem (e.g., the amino acid in a protein). The individual caps and cores are joined to form a whole cluster through sulfur-bridging bonds, which are the main framework for metal sulfide materials with diverse structure types, but in this case it only results in two enantiomeric cluster configurations *Cw* (*C*−*CC*−*C*) and *CCw* (*CC*−*C*−*CC*). The opposite chirality for the cap and core components is a result of the intramolecular interaction (C−H···π), and the cluster itself can then be considered to represent a secondary structure made up with distinct chiral cap and core units (like α-helix or β-sheet structure of a protein). Finally, the hydrogen bonding as an intermolecular driving force guides formation of a more complex hierarchical assembly, corresponding to a tertiary structure equal to, for example, the three-dimensional shape of a protein.

Density functional theory (DFT) geometry optimization obtained from X-ray single-crystal diffraction reveals the presence of a single hydride embedded in the Cu_5 core (Figure 3a). Without a hydride, DFT-relaxed atomic positions

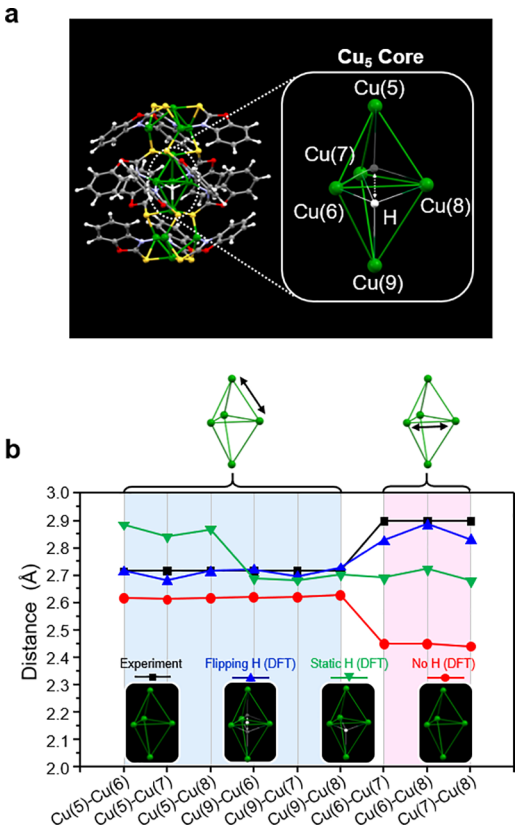

Figure 3. (a) A hydride located inside of the Cu_5 bipyramidal core is determined from density functional theory (DFT) geometry optimization of the model SB-Cu cluster. (b) Comparison of Cu−Cu distances between the X-ray structure and different models calculated from DFT. Cu atom labels are specified in a. More details can be found in the SI, Figure S22 and Table S11.

of the Cu_5 core atoms are substantially different from the experimentally derived positions (Figure 3b, "Experiment" vs "No H" plots). While better fits result when the H is located either above or below the Cu(1)−Cu(2)−Cu(3) plane (Figure 3b, "Static H" model), the best agreement is obtained when H is placed in plane with these three Cu atoms (Figure 3b, "Flipping H" model). Nudged elastic band calculations reveal that this transition state is only 50 meV higher in energy than the static H model. Molecular dynamics simulations (SI, Figure S25) confirm that at room temperature, hydrogen is resonating between the upper and the lower cavities on picosecond time scales, resulting in an averaging out of the Cu−Cu distances. The resulting positions show much better agreement with experimental data (Figure 3b, blue vs black plots) and also rationalizes the inability of detection by XRD since the hydrogen is partitioned between the two cavities.

In addition, without a hydrogen atom, DFT calculations result in cluster magnetization (SI, Figure S20), consistent with the mismatch between the number of Cu atoms and MBO ligands (13 Cu atoms and 12 MBO ligands). Experiments did

https://dx.doi.org/10.1021/jacs.0c04764
J. Am. Chem. Soc. 2020, 142, 14495−14503

not reveal any magnetic behavior in our structure (SI, Figure S27), and zeta-potential measurements (SI, Figure S28) support the neutrality of the whole cluster, suggesting that, in the absence of a central hydrogen atom, the electrons must be paired via one of the following mechanisms: (i) electrons could be transferred from one cluster to another to achieve pairing or (ii) additional electrons from cocrystallized counterions saturate the SB-Cu cluster. However, solubilizing the clusters to prevent their cross-talk did not show any magnetic behavior. DFT calculations on a pair of clusters confirmed that a charge-transferred configuration is 0.2 eV less stable than having unpaired spins on each cluster, irrespective of spin orientation. Similarly, careful analysis of the X-ray diffraction data did not reveal any cocrystallized counterions in the crystal. Thus, it is likely that a hydride (H^-) ion is present that neutralizes the charged $[Cu(MBO)_{12}]^+$ moiety and pairs the spins. Although confirmation of the single hydride would be difficult to detect from mass spectroscopy as the isotope distribution patterns for the $[M]^+$ ion with/without the single hydride are severely overlapped (SI, Figure S29), the presence of the hydride can be confirmed by ^1H NMR spectroscopy. While the ^1H NMR spectrum recorded at room temperature does not show an obvious hydride signal, the low-temperature NMR investigation at −60 °C reveals a weak and relatively broad peak at −1.32 ppm (SI, Figure S9), which can be assigned to the single hydride.[34] Formation of hydride in the copper reduction process during synthesis of copper clusters is very common.[34−36] Unfortunately, the location of the hydride atoms is extremely difficult to be unambiguously detected by X-ray diffraction due to the small scattering factor of hydrogen, and further confirmation of the hydride from neutron diffraction will be carried out in future work.

The HOMO and LUMO states of the structure fully relaxed with one hydrogen are localized primarily on the Cu core (Figure 4a), thus providing significant electron and hole overlap, consistent with detectable optical absorption and emission in the cluster (SI, Figures S4 and S5). In addition, the projected density of states (Figure 4b) shows a significant contribution of ligands (∼70%) to molecular orbitals, including the HOMO and LUMO, consistent with delocalization into the ligand shell observed in wave function plots. Frontier orbitals are predominantly built from d states of Cu and p states of O, C, N, and S. A reduced band gap is expected for conjugated ligands (phenyl rings with embedded O, N, and S), resulting in a band gap comparable to that of the Cu cluster. This is even more obvious in the molecular orbital composition plot (Figure 4c), clearly showing that Cu and ligands intermix and contribute to the same state (as opposed to being independent states lying close in energy but not intermixing) thanks to covalent coupling of the ligand to Cu through a sulfur bridge. The PDOS and state energy diagrams show a clean band gap without any strongly localized trap states. Nevertheless, the optical transitions calculation shows that the two lowest transitions (HOMO → LUMO and HOMO−1 → LUMO) are about 5 times weaker than those higher in energy (e.g., HOMO-2 → LUMO or HOMO → LUMO+1) (SI, Figure S26). This behavior can be traced back to the symmetry selection rules by examining the wave functions and their symmetry/antisymmetry.

X-ray absorption near-edge structure (XANES) analysis (Figure 5a, inset) reveals that the average oxidation state of Cu in the clusters was between 0 and +1 based on the comparison

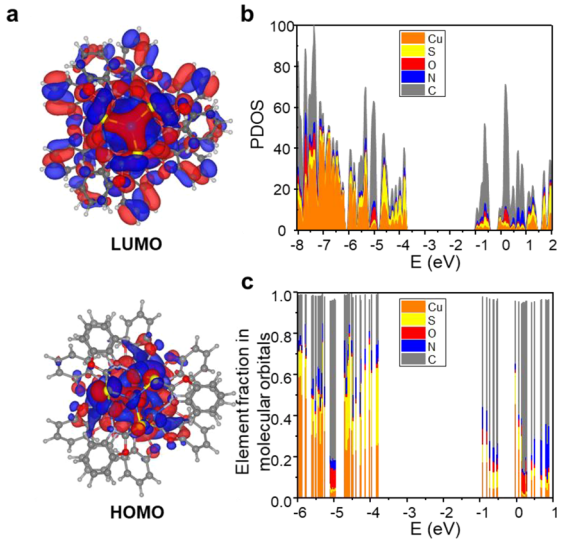

Figure 4. (a) HOMO and LUMO wave functions, (b) projected density of states (PDOS), and (c) molecular orbital composition plot for the SB-Cu cluster.

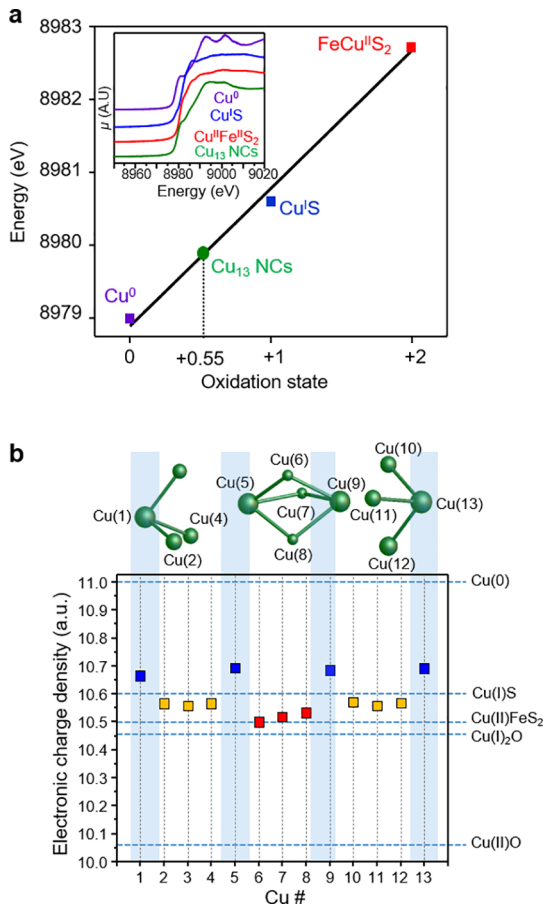

Figure 5. (a) XANES analysis to determine the oxidation state of Cu for SB-Cu clusters (normalized XANES spectra of Cu and three standards Cu(0), Cu(I)S, and Cu(II)FeS_2 are shown in the inset). (b) Electronic charge density for the Cu atom in the SB-Cu cluster compared with that in Cu(I)S, Cu(II)FeS_2, Cu(I)$_2$O, and Cu(II)O based on Bader analysis (a neutral Cu atom is arbitrarily set to have a maximum charge density of 11.00).

https://dx.doi.org/10.1021/jacs.0c04764
J. Am. Chem. Soc. 2020, 142, 14495−14503

with three standards Cu(0), Cu(I)S, and Cu(II)FeS_2. The choice of Cu(I) and Cu(II)FeS_2 lies in their similar Cu−S binding nature and coordination geometries as the SB-Cu cluster. Importantly, the synthesized sulfides according to the procedure reported have well-established oxidation states with monovalent and divalent coppers in CuS[37] and $CuFeS_2$,[38] respectively, in line with our experimental XANES spectra. The absence of the pre-edge peak for the SB-Cu clusters indicates a fully occupied 3d orbital of Cu (no 1s → 3d transition),[39] consistent with the NMR and magnetic results discussed previously. Extrapolation of the clusters' copper K-edge position relative to the standards (SI, Figures S28—S31) indicates the average oxidation state is +0.55 (Figure 5a), which is consistent with the X-ray photoelectron spectrum (SI, Figure S32). Considering the different coordination *n* environments in the structure, the 13 copper atoms are expected to vary between different oxidation states.

Bader analysis is a computational method for estimation of the relative charge density for atoms in a compound[40−43] (Figure 5b). The charge density partition for our SB-Cu cluster reveals that the three planar triangular Cu atoms in the Cu_5 core have the fewest electrons (higher oxidation state), while the apex coppers in both the cap and the core possess the most electrons (lowest oxidation states) overall, demonstrating an inhomogeneous charge distribution for the active metal atoms. It is encouraging that the SB-Cu clusters stabilize a partially metallic copper state because clusters containing Cu(0) are difficult to stabilize since they are more prone to oxidation than gold due to the lower half-cell reduction potential (0.52 vs 1.69 V for Cu(I)/Cu(0) and Au(I)/Au(0), respectively).[44−47] Here, we show that the SB-Cu clusters not only have a partial Cu(0) character but also display excellent stability in the open air, making them attractive for applications. Moreover, employment of the conjugated MBO ligand endows the SB-Cu clusters with electrical conductivity with the preliminary 2-probe electronic measurements showing that the SB-Cu clusters are conductive with a typical current−voltage (*I*−*V*) curve characteristic of semiconductors (SI, Figure S35). Full investigations of the electrical properties will be published in the future.

To investigate the stability and utility of the mixed-valence copper in the clusters we exposed them to electrocatalytic conditions. The SB-Cu clusters are active and stable as cathode catalysts for the oxygen reduction reaction (ORR). Compared to an N_2-saturated KOH electrolyte with a featureless voltammetric profile, in the presence of O_2 the SB-Cu clusters exhibit a larger cathodic current with the onset potential at approximately −0.3 V (versus Ag/AgCl), which can be assigned to the oxygen reduction reaction (Figure 6a). The double-layer response in N_2 and O_2 is different, which indicates that the SB-Cu cluster might undergo different electrochemical processes. The reaction kinetics investigated by rotating disk voltammetry (SI, Figure S33) produce linear Koutecky−Levich plots from −0.7 to −1.1 V (SI, Figure S34), from which the number of transferred electrons (*n*) per oxygen molecule can be calculated. At −0.7 V, each O_2 molecule gains 2.3 electrons (SI, Figure S35), suggesting formation of hydrogen peroxide as the major product with a small amount of water after the reduction of O_2. With more negative applied potentials, the value of *n* increases to 3.3 at −1.1 V, implying that water becomes the main product while hydrogen peroxide is the minor phase.[48−50] The SB-Cu electrocatalysts demonstrate surprisingly high durability for ORR: after 130 h the clusters retain about 70% of the initial current (Figure 6b), while other copper clusters reported are typically 2 orders of magnitude shorter in cycle life, only able to preserve their meaningful electrocatalytic activities for a few hours.[51,52] In addition, the SB-Cu clusters demonstrate electrocatalytic activity in carbon dioxide reduction, producing 78% H_2 and 20% CO as the major product at −1.05 V and a small amount of CH_4 as well (SI, Figure S36), which is in line with the trend observed for the high-energy, undercoordinated Cu atoms.[53]

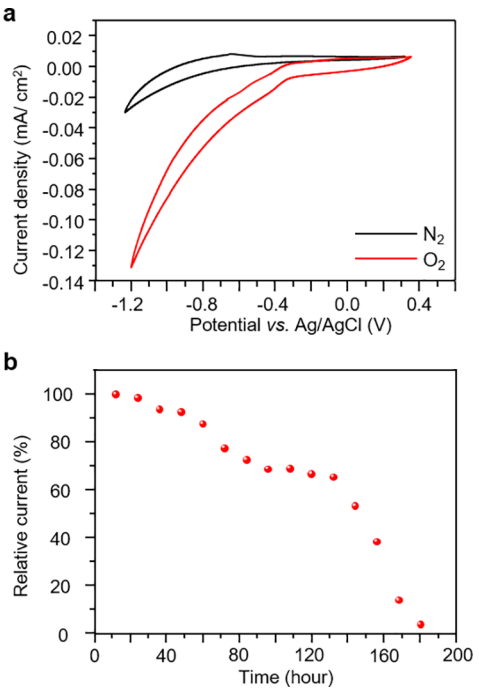

Figure 6. (a) Cyclic voltammograms of isolated SB-Cu clusters for ORR in N_2-saturated (black) and O_2-saturated (red) solutions of KOH (0.1M) (top). (b) Current−time chronoamperometric response of isolated SB-Cu clusters at −0.7 V in O_2-saturated KOH solution (0.1 M) at a rotation rate of 1600 rpm (bottom).

CONCLUSIONS

In this work, an ultrastable and conductive sulfur-bridged [Cu_4−Cu_5−Cu_4] cluster with a cap−core−cap structure was obtained. This cluster contains both sulfur−metal and metal−metal bonds, which are known to be the origins for many interesting chemistry/physical properties. Uniquely, the cap and core components in the cluster each have their own direction of either clockwise or counterclockwise, but only two chirality-specific enantiomeric clusters (*C*−*CC*−*C* or *CC*−*C*−*CC*) are produced. The hydrogen bonding and the intermolecular interaction further guide formation of a more complex hierarchical assembly composed of alternating enantiomers. This study reveals that clusters at the subnanoscale can also be smart as biomolecules to form structures in higher level complexity.

ASSOCIATED CONTENT

Supporting Information

The Supporting Information is available free of charge at https://pubs.acs.org/doi/10.1021/jacs.0c04764.

Additional file of crystallographic data (CIF)

Experimental details, synthesis, X-ray crystallographic procedures, UV−vis absorption spectroscopy, photo-

https://dx.doi.org/10.1021/jacs.0c04764
J. Am. Chem. Soc. 2020, 142, 14495−14503

luminescence analysis, X-ray photoelectron spectroscopy, dynamic light scattering, nuclear magnetic resonance, density functional theory simulation, X-ray absorption near-edge spectroscopy, and electrocatalytic activity evaluations for oxygen and carbon dioxide reduction reactions (PDF)

AUTHOR INFORMATION

Corresponding Author

Richard D. Robinson − *Department of Materials Science and Engineering, Cornell University, Ithaca, New York 14853, United States;* orcid.org/0000-0002-0385-2925; Email: rdr82@cornell.edu

Authors

Haixiang Han − *Department of Materials Science and Engineering, Cornell University, Ithaca, New York 14853, United States;* orcid.org/0000-0002-8465-9624

Yuan Yao − *Department of Materials Science and Engineering, Cornell University, Ithaca, New York 14853, United States*

Anuj Bhargava − *Department of Materials Science and Engineering, Cornell University, Ithaca, New York 14853, United States;* orcid.org/0000-0002-5961-6171

Zheng Wei − *Department of Chemistry, University at Albany, State University of New York, Albany, New York 12222, United States*

Zhichu Tang − *Department of Materials Science and Engineering, Cornell University, Ithaca, New York 14853, United States*

Jin Suntivich − *Department of Materials Science and Engineering, Cornell University, Ithaca, New York 14853, United States*

Oleksandr Voznyy − *Department of Physical and Environmental Sciences, University of Toronto Scarborough, Toronto, Ontario M1C 1A4, Canada;* orcid.org/0000-0002-8656-5074

Complete contact information is available at: https://pubs.acs.org/10.1021/jacs.0c04764

Notes

The authors declare no competing financial interest.

ACKNOWLEDGMENTS

This work was supported in part by the National Science Foundation (NSF) under award nos. CHE-1507753 and CHE-1665305. We thank Dr. Samantha N. MacMillan at Cornell University's Department of Chemistry and Chemical Biology X-ray Diffraction Facility for X-ray crystallographic data collection. We thank Ji Chen for Bader analysis and data interpretation. We thank Zheng Zhou for NMR investigation. Computations were performed on the Niagara supercomputer at the SciNet HPC Consortium. SciNet is funded by the Canada Foundation for Innovation, the Government of Ontario, Ontario Research Fund-Research Excellence, and the University of Toronto. The XANES investigation used beamline 7-BM (QAS) of the National Synchrotron Light Source II, a U.S. DOE Office of Science User Facility operated for the DOE Office of Science by Brookhaven National Laboratory under Contract No.DE-SC0012704. This work also made use of the Cornell Center for Materials Research Shared Facilities, which are supported through the NSF MRSEC (Materials Research Science and Engineering Centers) program (Grant DMR-1719875).

REFERENCES

(1) Bokov, K.; Steinberg, S. V. A Hierarchical Model for Evolution of 23s Ribosomal RNA. *Nature* **2009**, *457*, 977−980.

(2) Noller, H. F. Structure of Ribosomal Rna. *Annu. Rev. Biochem.* **1984**, *53*, 119−162.

(3) Shadish, J. A.; Benuska, G. M.; DeForest, C. A. Bioactive Site-Specifically Modified Proteins for 4d Patterning of Gel Biomaterials. *Nat. Mater.* **2019**, *18*, 1005−1014.

(4) Restuccia, A.; Seroski, D. T.; Kelley, K. L.; O'Bryan, C. S.; Kurian, J. J.; Knox, K. R.; Farhadi, S. A.; Angelini, T. E.; Hudalla, G. A. Hierarchical Self-Assembly and Emergent Function of Densely Glycosylated Peptide Nanofibers. *Commun. Chem.* **2019**, *2* (1), 53.

(5) Tanrikulu, I. C.; Forticaux, A.; Jin, S.; Raines, R. T. Peptide Tessellation Yields Micrometre-Scale Collagen Triple Helices. *Nat. Chem.* **2016**, *8*, 1008−1014.

(6) Brea, R. J.; Reiriz, C.; Granja, J. R. Towards Functional Bionanomaterials Based on Self-Assembling Cyclic Peptide Nanotubes. *Chem. Soc. Rev.* **2010**, *39*, 1448−1456.

(7) Miszta, K.; de Graaf, J.; Bertoni, G.; Dorfs, D.; Brescia, R.; Marras, S.; Ceseracciu, L.; Cingolani, R.; van Roij, R.; Dijkstra, M.; Manna, L. Hierarchical Self-Assembly of Suspended Branched Colloidal Nanocrystals into Superlattice Structures. *Nat. Mater.* **2011**, *10*, 872.

(8) Park, S. Y.; Lytton-Jean, A. K. R.; Lee, B.; Weigand, S.; Schatz, G. C.; Mirkin, C. A. DNA-Programmable Nanoparticle Crystallization. *Nature* **2008**, *451*, 553−556.

(9) Schreiber, R.; Do, J.; Roller, E.-M.; Zhang, T.; Schüller, V. J.; Nickels, P. C.; Feldmann, J.; Liedl, T. Hierarchical Assembly of Metal Nanoparticles, Quantum Dots and Organic Dyes Using DNA Origami Scaffolds. *Nat. Nanotechnol.* **2014**, *9*, 74−78.

(10) Xu, Y.; Qin, C.; Fei, J.; Yuan, T.; Li, G.; Wang, C.; Li, J. Fabrication of One-Dimensional Gold Hierarchical Nanostructures through Supramolecular Assembly. *Colloids Surf., A* **2018**, *541*, 52−57.

(11) Macfarlane, R. J.; Lee, B.; Jones, M. R.; Harris, N.; Schatz, G. C.; Mirkin, C. A. Nanoparticle Superlattice Engineering with DNA. *Science* **2011**, *334*, 204.

(12) Auyeung, E.; Li, T. I. N. G.; Senesi, A. J.; Schmucker, A. L.; Pals, B. C.; de la Cruz, M. O.; Mirkin, C. A. DNA-Mediated Nanoparticle Crystallization into Wulff Polyhedra. *Nature* **2014**, *505*, 73−77.

(13) Damasceno, P. F.; Engel, M.; Glotzer, S. C. Predictive Self-Assembly of Polyhedra into Complex Structures. *Science* **2012**, *337*, 453.

(14) Kalsin, A. M.; Fialkowski, M.; Paszewski, M.; Smoukov, S. K.; Bishop, K. J. M.; Grzybowski, B. A. Electrostatic Self-Assembly of Binary Nanoparticle Crystals with a Diamond-Like Lattice. *Science* **2006**, *312*, 420.

(15) Petty, J. T.; Zheng, J.; Hud, N. V.; Dickson, R. M. DNA-Templated Ag Nanocluster Formation. *J. Am. Chem. Soc.* **2004**, *126*, 5207−5212.

(16) Gwinn, E. G.; O'Neill, P.; Guerrero, A. J.; Bouwmeester, D.; Fygenson, D. K. Sequence-Dependent Fluorescence of DNA-Hosted Silver Nanoclusters. *Adv. Mater.* **2008**, *20*, 279−283.

(17) Chakraborty, S.; Babanova, S.; Rocha, R. C.; Desireddy, A.; Artyushkova, K.; Boncella, A. E.; Atanassov, P.; Martinez, J. S. A Hybrid DNA-Templated Gold Nanocluster for Enhanced Enzymatic Reduction of Oxygen. *J. Am. Chem. Soc.* **2015**, *137*, 11678−11687.

(18) Chen, Y.; Phipps, M. L.; Werner, J. H.; Chakraborty, S.; Martinez, J. S. DNA Templated Metal Nanoclusters: From Emergent Properties to Unique Applications. *Acc. Chem. Res.* **2018**, *51*, 2756−2763.

(19) Wu, Z.; Yao, Q.; Zang, S.; Xie, J. Directed Self-Assembly of Ultrasmall Metal Nanoclusters. *ACS Mater. Lett.* **2019**, *1*, 237−248.

(20) Zeng, C.; Chen, Y.; Kirschbaum, K.; Lambright, K. J.; Jin, R. Emergence of Hierarchical Structural Complexities in Nanoparticles and Their Assembly. *Science* **2016**, *354*, 1580.
(21) DeRosha, D. E.; Chilkuri, V. G.; Van Stappen, C.; Bill, E.; Mercado, B. Q.; DeBeer, S.; Neese, F.; Holland, P. L. Planar Three-Coordinate Iron Sulfide in a Synthetic [4Fe-3s] Cluster with Biomimetic Reactivity. *Nat. Chem.* **2019**, *11*, 1019−1025.
(22) Vilar-Vidal, N.; Rivas, J.; López-Quintela, M. A. Size Dependent Catalytic Activity of Reusable Subnanometer Copper(0) Clusters. *ACS Catal.* **2012**, *2*, 1693−1697.
(23) Wei, W.; Lu, Y.; Chen, W.; Chen, S. One-Pot Synthesis, Photoluminescence, and Electrocatalytic Properties of Subnanometer-Sized Copper Clusters. *J. Am. Chem. Soc.* **2011**, *133*, 2060−2063.
(24) Guo, Y.; Cao, F.; Lei, X.; Mang, L.; Cheng, S.; Song, J. Fluorescent Copper Nanoparticles: Recent Advances in Synthesis and Applications for Sensing Metal Ions. *Nanoscale* **2016**, *8*, 4852−4863.
(25) Wang, C.; Wang, C.; Xu, L.; Cheng, H.; Lin, Q.; Zhang, C. Protein-Directed Synthesis of Ph-Responsive Red Fluorescent Copper Nanoclusters and Their Applications in Cellular Imaging and Catalysis. *Nanoscale* **2014**, *6*, 1775−1781.
(26) Huang, H.; Li, H.; Wang, A.-J.; Zhong, S.-X.; Fang, K.-M.; Feng, J.-J. Green Synthesis of Peptide-Templated Fluorescent Copper Noclusters for Temperature Sensing and Cellular Imaging. *Analyst* **2014**, *139*, 6536−6541.
(27) Gao, X.; He, S.; Zhang, C.; Du, C.; Chen, X.; Xing, W.; Chen, S.; Clayborne, A.; Chen, W. Single Crystal Sub-Nanometer Sized $Cu_6(Sr)_6$ Clusters: Structure, Photophysical Properties, and Electrochemical Sensing. *Adv. Sci.* **2016**, *3*, 1600126.
(28) Wang, N.; Zhao, D.; Wang, J.; Zhang, Y.; Wang, M.; Gao, Y.; Li, F.; Wang, J.; Bu, Z.; Rao, Z.; Wang, X. Architecture of African Swine Fever Virus and Implications for Viral Assembly. *Science* **2019**, *366*, 640−644.
(29) Jin, R.; Zeng, C.; Zhou, M.; Chen, Y. Atomically Precise Colloidal Metal Nanoclusters and Nanoparticles: Fundamentals and Opportunities. *Chem. Rev.* **2016**, *116*, 10346−10413.
(30) Zhang, L. L.-M.; Mak, T. C. W. Temperature-Mediated Template Release: Facile Growth of Copper(I) Mixed Ethynediide/Isopropylethynide Nanoclusters. *Angew. Chem., Int. Ed.* **2017**, *56*, 16228−16232.
(31) Higgs, T. C.; Bailey, P. J.; Parsons, S.; Tasker, P. A. Facile Syntheses of Copper(I) Alkynyl Clusters Stabilized by Hexafluoroacetylacetonate (Hfac) Ligands: The Structure of $[Cu_{26}(Hfac)_{11}(1\text{-Pentynyl})_{15}]$. *Angew. Chem., Int. Ed.* **2002**, *41*, 3038−3041.
(32) Wilson, K. A.; Kellie, J. L.; Wetmore, S. D. DNA−Protein Π-Interactions in Nature: Abundance, Structure, Composition and Strength of Contacts between Aomatic Amino Acids and DNA Nucleobases or Deoxyribose Sugar. *Nucleic Acids Res.* **2014**, *42*, 6726−6741.
(33) Van Treeck, B.; Parker, R. Emerging Roles for Intermolecular Rna-Rna Interactions in Rnp Assemblies. *Cell* **2018**, *174*, 791−802.
(34) Dhayal, R. S.; Liao, J.-H.; Lin, Y.-R.; Liao, P.-K.; Kahlal, S.; Saillard, J.-Y.; Liu, C. W. A Nanospheric Polyhydrido Copper Cluster of Elongated Triangular Orthobicupola Array: Liberation of H_2 from Solar Energy. *J. Am. Chem. Soc.* **2013**, *135*, 4704−4707.
(35) Ghosh, A.; Huang, R.-W.; Alamer, B.; Abou-Hamad, E.; Hedhili, M. N.; Mohammed, O. F.; Bakr, O. M. $[Cu_{61}(Stbu)_{26}s_6cl_6h_{14}]^+$: A Core−Shell Superatom Nanocluster with a Quasi-*J*36 Cu_{19} Core and an "18-Crown-6" Metal-Sulfide-Like Stabilizing Belt. *ACS Mater. Lett.* **2019**, *1*, 297−302.
(36) Nguyen, T.-A. D.; Jones, Z. R.; Leto, D. F.; Wu, G.; Scott, S. L.; Hayton, T. W. Ligand-Exchange-Induced Growth of an Atomically Precise Cu_{29} Nanocluster from a Smaller Cluster. *Chem. Mater.* **2016**, *28*, 8385−8390.
(37) Xie, Y.; Riedinger, A.; Prato, M.; Casu, A.; Genovese, A.; Guardia, P.; Sottini, S.; Sangregorio, C.; Miszta, K.; Ghosh, S.; Pellegrino, T.; Manna, L. Copper Sulfide Nanocrystals with Tunable Composition by Reduction of Covellite Nanocrystals with Cu^+ Ions. *J. Am. Chem. Soc.* **2013**, *135*, 17630−17637.
(38) Todd, E. C.; Sherman, D. M.; Purton, J. A. Surface Oxidation of Chalcopyrite ($CuFeS_2$) under Ambient Atmospheric and Aqueous (pH 2−10) Conditions: Cu, Fe L- and O K-Edge X-Ray Spectroscopy. *Geochim. Cosmochim. Acta* **2003**, *67* (12), 2137−2146.
(39) Sarangi, R.; Aboelella, N.; Fujisawa, K.; Tolman, W. B.; Hedman, B.; Hodgson, K. O.; Solomon, E. I. X-Ray Absorption Edge Spectroscopy and Computational Studies on $Lcuo_2$ Species: Superoxide−Cuii Versus Peroxide−Cuiii Bonding. *J. Am. Chem. Soc.* **2006**, *128*, 8286−8296.
(40) Yu, M.; Trinkle, D. R. Accurate and Efficient Algorithm for Bader Charge Integration. *J. Chem. Phys.* **2011**, *134*, 064111.
(41) Tang, W.; Sanville, E.; Henkelman, G. A Grid-Based Bader Analysis Algorithm without Lattice Bias. *J. Phys.: Condens. Matter* **2009**, *21* (8), 084204.
(42) Sanville, E.; Kenny, S. D.; Smith, R.; Henkelman, G. Improved Grid-Based Algorithm for Bader Charge Allocation. *J. Comput. Chem.* **2007**, *28*, 899−908.
(43) Henkelman, G.; Arnaldsson, A.; Jónsson, H. A Fast and Robust Algorithm for Bader Decomposition of Charge Density. *Comput. Mater. Sci.* **2006**, *36*, 354−360.
(44) Nguyen, T.-A. D.; Jones, Z. R.; Goldsmith, B. R.; Buratto, W. R.; Wu, G.; Scott, S. L.; Hayton, T. W. A Cu_{25} Nanocluster with Partial Cu(0) Character. *J. Am. Chem. Soc.* **2015**, *137*, 13319−13324.
(45) Yuan, P.; Chen, R.; Zhang, X.; Chen, F.; Yan, J.; Sun, C.; Ou, D.; Peng, J.; Lin, S.; Tang, Z.; Teo, B. K.; Zheng, L. S.; Zheng, N. Ether-Soluble Cu_{53} Nanoclusters as an Effective Precursor of High-Quality Cui Films for Optoelectronic Applications. *Angew. Chem., Int. Ed.* **2019**, *58*, 835−839.
(46) Bezman, S. A.; Churchill, M. R.; Osborn, J. A.; Wormald, J. Preparation and Crystallographic Characterization of a Hexameric Triphenylphosphinecopper Hydride Cluster. *J. Am. Chem. Soc.* **1971**, *93*, 2063−2065.
(47) Nguyen, T.-A. D.; Cook, A. W.; Wu, G.; Hayton, T. W. Subnanometer-Sized Copper Clusters: A Critical Re-Evaluation of the Synthesis and Characterization of $Cu_8(Mpp)_4$ (HMpp = 2-Mercapto-5-N-Propylpyrimidine). *Inorg. Chem.* **2017**, *56*, 8390−8396.
(48) Yamamoto, K.; Imaoka, T.; Chun, W.-J.; Enoki, O.; Katoh, H.; Takenaga, M.; Sonoi, A. Size-Specific Catalytic Activity of Platinum Clusters Enhances Oxygen Reduction Reactions. *Nat. Chem.* **2009**, *1*, 397.
(49) Liu, M.; Zhao, Z.; Duan, X.; Huang, Y. Nanoscale Structure Design for High-Performance Pt-Based Orr Catalysts. *Adv. Mater.* **2019**, *31*, 1802234.
(50) Liang, Y.; Li, Y.; Wang, H.; Zhou, J.; Wang, J.; Regier, T.; Dai, H. Co_3o_4 Nanocrystals on Graphene as a Synergistic Catalyst for Oxygen Reduction Reaction. *Nat. Mater.* **2011**, *10*, 780−786.
(51) Wu, Z.; Li, Y.; Liu, J.; Lu, Z.; Zhang, H.; Yang, B. Colloidal Self-Assembly of Catalytic Copper Nanoclusters into Ultrathin Ribbons. *Angew. Chem., Int. Ed.* **2014**, *53*, 12196−12200.
(52) Du, C.; Gao, X.; Chen, W. Recent Developments in Copper-Based, Non-Noble Metal Electrocatalysts for the Oxygen Reduction Reaction. Chinese. *J. Catal.* **2016**, *37*, 1049−1061.
(53) Reske, R.; Mistry, H.; Behafarid, F.; Roldan Cuenya, B.; Strasser, P. Particle Size Effects in the Catalytic Electroreduction of CO_2 on Cu Nanoparticles. *J. Am. Chem. Soc.* **2014**, *136*, 6978−6986.

https://dx.doi.org/10.1021/jacs.0c04764
J. Am. Chem. Soc. 2020, 142, 14495−14503